

¹ Magnetospheric Cavity Modes Driven by Solar Wind ² Dynamic Pressure Fluctuations

S. G. Claudepierre,¹ M. Wiltberger,² S. R. Elkington,³ W. Lotko,⁴ and M. K.

Hudson¹

arXiv:1010.3984v1 [physics.space-ph] 19 Oct 2010

S. G. Claudepierre and M. K. Hudson, Department of Physics and Astronomy, Dartmouth College, Hanover, NH 03755, USA. (Seth.G.Claudepierre@dartmouth.edu)

M. Wiltberger, NCAR, High Altitude Observatory, Boulder, CO 80301, USA.

S. R. Elkington, LASP, University of Colorado, Boulder, CO 80303, USA.

W. Lotko, Thayer School of Engineering, Dartmouth College, Hanover, NH 03755, USA.

¹Department of Physics and Astronomy,

3 We present results from Lyon-Fedder-Mobarry (LFM) global, three-dimensional
4 magnetohydrodynamic (MHD) simulations of the solar wind-magnetosphere in-
5 teraction. We use these simulations to investigate the role that solar wind dy-
6 namic pressure fluctuations play in the generation of magnetospheric ultra-low
7 frequency (ULF) pulsations. The simulations presented in this study are driven
8 with idealized solar wind input conditions. In four of the simulations, we intro-
9 duce monochromatic ULF fluctuations in the upstream solar wind dynamic pres-
10 sure. In the fifth simulation, we introduce a continuum of ULF frequencies in
11 the upstream solar wind dynamic pressure fluctuations. In this numerical exper-
12 iment, the idealized nature of the solar wind driving conditions allows us to study
13 the magnetospheric response to only a fluctuating upstream dynamic pressure,

Dartmouth College, Hanover, New Hampshire,

USA

²National Center for Atmospheric Research,
High Altitude Observatory, Boulder, Colorado,

USA

³Laboratory for Atmospheric and Space
Physics, University of Colorado, Boulder,
Colorado, USA

⁴Thayer School of Engineering, Dartmouth
College, Hanover, New Hampshire, USA

14 while holding all other solar wind driving parameters constant. The simulation
15 results suggest that ULF fluctuations in the solar wind dynamic pressure can drive
16 magnetospheric ULF pulsations in the electric and magnetic fields on the day-
17 side. Moreover, the simulation results suggest that when the driving frequency
18 of the solar wind dynamic pressure fluctuations matches one of the natural fre-
19 quencies of the magnetosphere, magnetospheric cavity modes can be energized.

1. Introduction

Several observational studies suggest that some dayside magnetospheric ultra-low frequency (ULF) pulsations may be directly driven by ULF fluctuations in the solar wind dynamic pressure. For example, *Kepko and Spence* [2003] examine six events where discrete ULF fluctuations are observed in the solar wind dynamic pressure. The authors show a one-to-one correspondence between these solar wind dynamic pressure fluctuations and discrete spectral peaks in dayside GOES magnetic field data. The authors argue that the dayside magnetospheric ULF pulsations are directly driven by the corresponding solar wind dynamic pressure fluctuations. Other observational studies [*Sibeck et al.*, 1989; *Korotova and Sibeck*, 1995; *Matsuoka et al.*, 1995; *Han et al.*, 2007] also suggest that solar wind dynamic pressure fluctuations can directly drive dayside magnetic field ULF pulsations. Very recent work [*Viall et al.*, 2009] concludes that approximately half of the variations observed in magnetospheric ULF waves are likely directly driven by solar wind dynamic pressure fluctuations. In this study we investigate, through the use of global magnetohydrodynamic (MHD) simulations, the magnetospheric response to ULF solar wind dynamic pressure (henceforth, p_{dyn}) fluctuations. Here, ‘ULF’ refers to frequencies in the 0.5 to 50 mHz range (Pc3-Pc5 bands; *Jacobs et al.* [1964]), though we make no distinction between continuous and irregular magnetospheric pulsations.

2. Methodology

The details of the Lyon-Fedder-Mobarry (LFM) simulation code, the computational grid, and the numerical techniques used to solve the single-fluid ideal MHD equations can be found in *Lyon et al.* [2004]. The solar wind input conditions form the outer boundary condition in the LFM simulation. For the inner boundary condition, the magnetospheric portion of the code

40 couples to an empirical ionospheric model, which forms a two-way coupling between the sim-
41 ulation ionosphere and magnetosphere [Wiltberger *et al.*, 2009]. The LFM simulation does not
42 contain a plasmaspheric model and, thus, number densities in the simulation inner magneto-
43 sphere are lower than what is typically observed in the real magnetosphere. Also, as discussed
44 in Lyon *et al.* [2004], the LFM utilizes the Boris correction when solving the ideal MHD equa-
45 tions, where the speed of light is replaced by a smaller value to increase the allowable time step.
46 The simulation code remains stable, however, when wave propagation speeds exceed the as-
47 sumed speed of light, roughly 1,100 km/s in the LFM inner magnetosphere. We present results
48 from five LFM simulations: four driven by monochromatic upstream p_{dyn} fluctuations and one
49 driven by a continuum of frequencies in the upstream p_{dyn} fluctuations.

50 Solar wind dynamic pressure is not an explicit input in the LFM simulation and we choose
51 to introduce the dynamic pressure fluctuations via the upstream number density component, as
52 opposed to the velocity component. Solar wind observations typically show that p_{dyn} variations
53 are carried by the solar wind number density, and not the velocity [e.g. Kepko and Spence,
54 2003; Han *et al.*, 2007]. For the four monochromatic simulations, we impose a number density
55 time series, $n(t)$, at the LFM upstream boundary at $x = 30 R_E$ of the form: $n(t) = n_0 +$
56 $\delta n \sin(\omega t)$. The four monochromatic driving frequencies chosen for analysis in this study are
57 5, 10, 18, and 25 mHz and the background number density, n_0 , is 5 particles/cm³. In the
58 5 and 10 mHz simulations, $\delta n = 1$ (20% oscillation amplitude); in the 18 mHz simulation,
59 $\delta n = 1.5$ (30% oscillation amplitude); and in the 25 mHz simulation, $\delta n = 2$ (40% oscillation
60 amplitude). The larger oscillation amplitudes for the input time series in the 18 mHz and 25
61 mHz runs are used to combat the effects of a numerical attenuation/filtering of higher frequency

62 components in the LFM simulation. For the fifth simulation, we impose a continuum of ULF
 63 frequencies in the input number density time series: $n(t) = n_0 + 0.05 \sum_j \sin(\omega_j t + \phi_j)$. Here,
 64 we create an input spectrum with fluctuations in the 0 to 50 mHz band with a 0.1 mHz spacing
 65 between frequency components (j ranges from 0 to 500) and we add a random phase, ϕ_j , to each
 66 frequency component. The value of 0.05 in the above equation is chosen so that the root-mean
 67 square (*RMS*) amplitude of the continuum input number density time series is roughly equal to
 68 that of the monochromatic input number density time series (with 20% oscillation amplitudes).
 69 In addition, in all five simulations, we introduce an appropriate out of phase oscillation in the
 70 input sound speed time series, so as to hold the thermal pressure constant in the upstream solar
 71 wind ($p_{th} \propto nC_s^2$). The background sound speed upon which the out of phase oscillation is
 72 imposed is 40 km/s. The remaining idealized solar wind input parameters are the same in all
 73 five simulations and held constant for the entire duration (4 hours) of the simulations: $\mathbf{B} =$
 74 $(0,0,-5)$ nT and $\mathbf{v} = (-600,0,0)$ km/s.

75 The power spectral density (*PSD*) of the continuum simulation input p_{dyn} time series is
 76 shown as the red trace in the inset panel in Figure 1a. Note the relatively uniform distribution of
 77 wave power over the 0 to 50 mHz frequency band. The blue trace in the inset panel shows the
 78 *PSD* of the p_{dyn} time series taken at $(20,0,0) R_E$ in the solar wind (GSM coordinates are used
 79 throughout) in the continuum simulation. Comparing the red and blue traces, we see that the
 80 spectral profile imposed at the upstream boundary (red trace) has been significantly altered by
 81 the time the fluctuations reach $(20,0,0) R_E$ (blue trace). This filtering/attenuation of the higher
 82 frequency spectral components, to be discussed in a follow-up paper, is an expected artifact of
 83 the numerics in the LFM [John Lyon, *personal communication*, 2008]. Nonetheless, there is

84 significant ULF wave power in the 0 to 20 mHz frequency band in the upstream p_{dyn} driving,
 85 which is the spectral profile that drives the magnetosphere.

86 The filtering/attenuation of the input time series in the continuum simulation results in up-
 87 stream driving at $(20,0,0) R_E$ on the order of 13%, reduced from the roughly 20% value imposed
 88 at the upstream boundary (in the *RMS* sense described above). As the inset panel in Figure 1a
 89 suggests, the filtering/attenuation reduces the amplitude of the upstream p_{dyn} driving at $(20,0,0)$
 90 R_E to 24% in the 18 mHz simulation (input = 30%) and 15% in the 25 mHz simulation (input
 91 = 40%). Finally, we note that upstream p_{dyn} driving in the 13-24% range is reasonable when
 92 compared with the observational work discussed above and is at the lower end of what has been
 93 reported.

3. Simulation Results

94 In all five simulations, the upstream p_{dyn} fluctuations launch earthward propagating compres-
 95 sional MHD waves near the subsolar bow shock. These waves propagate through the mag-
 96 netosheath and then enter the magnetosphere near the subsolar magnetopause and propagate
 97 earthward through the dayside (not shown here). We examine the magnetospheric response in
 98 the equatorial plane in terms of the compressional magnetic and electric field components, B_z
 99 and E_φ . Along the noon meridian, the magnetospheric response in terms of B_z and E_φ fluctua-
 100 tion amplitude is roughly an order of magnitude greater than in the other field components.

101 The green trace in Figure 1a shows the magnetospheric response to the upstream p_{dyn} fluctu-
 102 ations in the continuum simulation. Here, we plot power spectral density of the E_φ time series
 103 taken at $(5.4, 0, 0) R_E$ on the noon meridian. Note the clear preferential frequency in the mag-
 104 netospheric response centered near 10 mHz. Comparing the fine structure in the spectral profile

105 of the p_{dyn} fluctuations and the magnetospheric response near 10 mHz shows a one-to-one cor-
106 respondence between the two traces. This suggests that the fluctuations in the magnetospheric
107 E_{φ} are driven by the p_{dyn} fluctuations. Moreover, the fact that the magnetospheric response
108 is strongly peaked near 10 mHz suggests that the magnetosphere is responding resonantly to
109 the upstream p_{dyn} fluctuations, which contain a continuum of ULF frequencies. Although the
110 magnetospheric response falls off sharply away from 10 mHz, one could perhaps argue that the
111 response near 10 mHz is due to local peaks in the upstream driving spectrum near 10 mHz. The
112 local peaks and valleys in the upstream driving spectrum are the result of the random phasing in
113 the input time series and the discretization of the signal. We have conducted analogous simula-
114 tions to the continuum simulation presented here, with only the random phasing changed, which
115 moves the location of the local peaks and valleys in the upstream p_{dyn} driving spectrum. These
116 simulations also show a magnetospheric response that is strongly peaked near 10 mHz. Thus,
117 the magnetospheric response does not depend on the location of the local peaks and valleys in
118 the upstream driving spectrum.

119 To obtain a more global picture of the magnetospheric response, in Figure 1b we plot the
120 E_{φ} PSD along the entire noon meridian in the continuum simulation. Here, distance along the
121 noon meridian is plotted on the horizontal axis from $2.2 R_E$ (the inner boundary of the LFM
122 simulation) to $9 R_E$. The subsolar magnetopause is located near $8.6 R_E$ on the noon meridian,
123 though the magnetopause moves roughly $\pm 0.25 R_E$ about this location, due to the upstream
124 p_{dyn} oscillations. This radial motion of the magnetopause is indicated by the shaded region in
125 the figure. Note that the green trace in Figure 1a can be extracted from Figure 1b by taking a
126 vertical cut at $5.4 R_E$. The spectral profile along the entire noon meridian again shows a clear

127 preferential frequency near 10 mHz for the magnetospheric response. Note that the frequency
 128 of the magnetospheric response does not change significantly with radial distance. However,
 129 the amplitude of the response near 10 mHz does depend on radial distance, with the maximum
 130 in wave power occurring between 5 and 6 R_E . Finally, we note that there is an enhancement in
 131 the E_φ PSD near 6 mHz, that peaks just earthward of the magnetopause, and decays rapidly in
 132 the earthward direction. This is due to a local peak in the solar wind p_{dyn} fluctuations near 6
 133 mHz (Figure 1a, blue trace) and the fact that this local peak in the driving spectrum lies near a
 134 resonant frequency of the magnetosphere.

135 The results from the continuum simulation also suggest a secondary preferential frequency
 136 to the magnetospheric response, centered near 18 mHz. However, the upstream driving in the
 137 continuum simulation near 18 mHz is weaker than the driving near 10 mHz, due to the filter-
 138 ing/attenuation described above. Thus, the amplitude of the secondary magnetospheric response
 139 is weaker than the primary response near 10 mHz, and is not entirely resolved in Figure 1b due
 140 to the color scale used. As we will see below, the amplitude of the secondary response near 18
 141 mHz has two local maxima along the noon meridian, near 4 and 7 R_E , in contrast with one local
 142 maximum for the amplitude of the primary (10 mHz) response between 5 and 6 R_E .

143 In Figure 2, we plot radial profiles of E_φ (top row) and B_z (bottom row) root-integrated
 144 power along the noon meridian for the five simulations in this study (columns). Root-
 145 integrated power (RIP), plotted on the vertical axis in each of the 10 panels, is defined as:
 146 $RIP = (\int_{f_a}^{f_b} P(f)df)^{\frac{1}{2}}$, where $P(f)$ is the power spectral density of the time series under con-
 147 sideration and the integration is carried out over a given frequency band of interest, $[f_a, f_b]$. In
 148 the four monochromatic simulations (Figure 2, first four columns), the RIP is integrated over

149 the *driving band*, which we define as the 1 mHz frequency band centered on the driving fre-
150 quency. In the the continuum simulation (last column), two *RIP* traces are shown, as there is
151 no driving band in the continuum simulation. The solid trace is integrated over the frequency
152 band [7,12] mHz, to pick up the primary spectral peak near 10 mHz, while the dashed trace is
153 integrated over the frequency band [15,20] mHz to pick up the secondary spectral peak near 18
154 mHz. In each of the 10 panels, distance along the noon meridian is plotted on the horizontal
155 axis and the location of the subsolar magnetopause is indicated by the shaded regions near 8.5
156 R_E .

157 The five B_z panels in the bottom row of Figure 2 show a strong amplitude maximum in B_z
158 oscillation amplitude near the magnetopause that extends beyond the vertical scales used in the
159 plots (the traces extend to a value on the order of 25 nT). These strong oscillation amplitudes
160 near the magnetopause are due to the radial motion of the magnetopause and the subsequent
161 changing dayside magnetopause current. As a side note, effects due to the LFM grid are clearly
162 visible in the five B_z panels in the bottom row of Figure 2. For example, in the 5 mHz simulation
163 (bottom row, first panel) there is a ‘sawtooth’ like structure in the radial profile between 5 and 7
164 R_E . We do not attribute any physical significance to these features.

4. Discussion

165 The simulation results presented above suggest a resonant response of the magnetosphere
166 to solar wind dynamic pressure fluctuations, with a standing wave structure along the noon
167 meridian. The dependence of the magnetospheric response on the driving frequency can be
168 explained by interpreting the simulation results as signatures of magnetospheric cavity mode
169 oscillations [e.g. *Kivelson and Southwood, 1985*].

170 In the simplest interpretation, magnetospheric MHD cavity modes can be thought of as stand-
 171 ing waves in the electric and magnetic fields between a cavity inner and outer boundary. We con-
 172 sider the magnetopause to be the cavity outer boundary and the LFM simulation inner bound-
 173 ary at $2.2 R_E$ to be the cavity inner boundary. For the moment, we consider perfect conduc-
 174 tor boundary conditions at the simulation inner boundary and magnetopause ($E_y, \partial_x B_z \rightarrow 0$).
 175 These boundary conditions impose half-wavelength standing waves in the radial direction be-
 176 tween the simulation inner boundary and the magnetopause. Returning to the noon meridian
 177 radial profiles in Figure 2, we see that the simulation results support this standing wave inter-
 178 pretation. We argue that the E_φ and B_z radial profiles in the 10 mHz run (Figure 2, second
 179 column) are the signatures of the $n = 1$ cavity mode. Near the simulation inner boundary and
 180 magnetopause, E_φ has oscillation amplitude nodes and B_z has oscillation amplitude antinodes.
 181 Moreover, between the boundaries, E_φ has one oscillation amplitude antinode and B_z has one
 182 oscillation amplitude node, near $6 R_E$, all consistent with an $n = 1$ standing wave along the
 183 noon meridian. Note that the continuum simulation results suggest that the fundamental fre-
 184 quency of the magnetospheric cavity is near 10 mHz. Thus, the upstream driving frequency
 185 in the 10 mHz monochromatic simulation is near the fundamental resonant frequency of the
 186 magnetospheric cavity and the $n = 1$ radial eigenmode is excited.

187 In the 5 mHz simulation, we argue that a cavity mode is not excited, which is supported by
 188 the continuum simulation results. The radial profile of E_φ along the noon meridian in the 5
 189 mHz simulation (Figure 2, top row, first column) suggests an evanescent decay of wave power,
 190 with E_φ wave power peaking just earthward of the magnetopause and decaying rapidly in the
 191 earthward direction. Monochromatic simulations with 1 mHz and 3 mHz driving, analogous to

192 those presented here, show similar radial profiles in E_φ and B_z oscillation amplitude along the
193 noon meridian. Thus, we argue that this is the characteristic behavior of dayside compressional
194 magnetospheric disturbances under fluctuating solar wind p_{dyn} driving when cavity modes are
195 not excited, an evanescent decay of wave energy earthward of the magnetopause. Finally, we
196 note that the excitation of $n = 1$ cavity mode in the 10 mHz simulation is also able to explain
197 the stronger E_φ response amplitude under 10 mHz monochromatic driving when compared
198 with 5 mHz monochromatic driving. The peak value of E_φ oscillation amplitude along the
199 noon meridian is roughly 3.0 mV/m in the 5 mHz simulation, whereas it is roughly 3.7 mV/m
200 in the 10 mHz simulation. The only difference in the upstream driving in the two simulations is
201 the driving frequency. Thus, the magnetosphere responds resonantly to the p_{dyn} fluctuations in
202 the 10 mHz run and passively in the 5 mHz run.

203 We now consider the radial profiles of E_φ and B_z wave power in the 18 mHz and 25 mHz
204 monochromatic simulations. We argue that in the 18 mHz simulation the $n = 2$ cavity mode
205 is excited. Again, at the simulation inner boundary and magnetopause, E_φ has oscillation am-
206 plitude nodes, whereas B_z has amplitude antinodes. Moreover, near 4 and 7 R_E , E_φ has two
207 oscillation amplitude antinodes, whereas B_z has two nodes. As discussed above, the continuum
208 simulation results suggest that the frequency for an $n = 2$ oscillation lies near 18 mHz, which
209 is the driving frequency in the 18 mHz simulation. Similarly, in the 25 mHz simulation, we
210 argue that the $n = 3$ cavity mode is excited. In the E_φ profile, we see three clear oscillation
211 amplitude antinodes near 4, 6 and 8 R_E . Two of the three corresponding nodes in the B_z profile
212 are resolved near 4 and 7 R_E . The $n = 3$ interpretation also requires a third B_z node (likely
213 between 4 and 7 R_E) that is not resolved in the simulation. We note that the B_z profile suggests

214 that the RIP value for the unresolved node should be less than 1 nT. This would correspond
 215 to a peak-to-peak oscillation amplitude of roughly 2 nT or less, which is small when compared
 216 with background values on the order of 100's of nT. The LFM grid resolution (roughly 0.25
 217 R_E here) coupled with the small oscillation amplitude may make it difficult to resolve three
 218 distinct B_z nodes in an $\approx 3 R_E$ range. The E_φ profile is consistent with the $n = 3$ cavity mode
 219 interpretation. Finally, we note that the radial profiles from the continuum simulation, when
 220 integrated around 10 mHz (solid trace) and 18 mHz (dashed trace), look qualitatively similar
 221 to the profiles in the 10 mHz and 18 mHz monochromatic simulations, respectively. This sug-
 222 gests that the $n = 1$ and $n = 2$ radial eigenmodes are simultaneously excited in the continuum
 223 simulation.

The results from the continuum simulation suggest that the fundamental frequency of the
 magnetospheric cavity configuration is near 10 mHz. To derive an alternate estimate, we con-
 sider the cavity frequency in a simple box geometry configuration [e.g. *Wright*, 1994]:

$$f_n = \frac{V_A}{2a}n \quad \text{for } n = 1, 2, 3, \dots \quad (1)$$

224 where V_A is the Alfvén speed in the box, a is the box length in the X direction, and n is the
 225 quantization number. Here, we envision the box coordinates, (X, Y, Z) as the radial, azimuthal
 226 and field aligned directions in the LFM. The above equation for f_n assumes perfect conductor
 227 boundary conditions in the X -direction ($E_Y, \partial_X B_Z \rightarrow 0$). To evaluate the fundamental fre-
 228 quency in the box configuration, we consider $n = 1$ and only compare with LFM results from
 229 the 10 mHz and continuum simulations, as these are the only two simulations where the fun-
 230 damental radial eigenmode is excited. We evaluate the fundamental frequency, f_1 , in the box
 231 with $a = 6.4 R_E$, the distance from the simulation inner boundary to the magnetopause, along

232 the noon meridian. A value for the constant Alfvén speed in the box, V_A , must also be chosen.
 233 By tracking the compressional wave fronts in the 10 mHz simulation, as they move earthward
 234 from the subsolar magnetopause along the noon meridian, we compute a phase speed, $V_{ph,x}$, of
 235 roughly 1,750 km/s. With this estimate for V_A , we obtain $f_1 \approx 22$ mHz. For quarter-wavelength
 236 modes in the X direction, the $2a$ in Equation (1) is replaced by $4a$ and the fundamental cavity
 237 frequency is $f_1 \approx 11$ mHz, close to the result suggested by the continuum simulation. The fact
 238 that the quarter-wavelength fundamental cavity frequency is closer to 10 mHz than the half-
 239 wavelength estimate and the fact that the electric field oscillation amplitude does not go entirely
 240 to zero at the magnetopause both suggest that quarter-wavelength modes may be a more appro-
 241 priate boundary condition at the magnetopause.

242 As discussed in Section 2, the speed of light in the LFM is set to an artificially low value,
 243 which limits the Alfvén wave propagation speed. Above, we computed a phase speed of roughly
 244 1,750 km/s for the p_{dyn} -driven waves in the 10 mHz simulation, which exceeds the speed of light
 245 in the simulation. Thus, the wave propagation characteristics of the p_{dyn} -driven waves are ef-
 246 fected by the Boris correction. The Boris correction compensates for neglect of the displacement
 247 current in the ideal MHD equations, which reduces the phase speed when $V_A \sim c$.

248 Finally, we emphasize that the results presented in this study do not necessarily imply that
 249 the fundamental cavity frequency of the real magnetosphere is near 10 mHz. A key factor con-
 250 trolling the fundamental frequency of the magnetospheric cavity is the Alfvén speed profile.
 251 The LFM simulations presented in this study do not have a plasmaspheric model and, thus,
 252 have number densities in the dayside equatorial plane that are much lower than in the real mag-
 253 netosphere. For example, a typical value for the LFM number density near $(5,0,0) R_E$ is 0.1

254 particles/cm³. A more realistic LFM number density profile in the equatorial plane, under devel-
255 opment, would significantly lower the fundamental cavity frequency of the LFM magnetosphere
256 (e.g. Equation (1)). For this reason, we do not compare the LFM simulation results with the
257 observations of magnetospheric ULF waves driven by p_{dyn} fluctuations discussed in Section 1.
258 The observational work [e.g. *Kepko and Spence, 2003*] typically looks at frequencies less than
259 5 mHz, while we have shown that the lowest cavity mode frequency that the LFM supports, for
260 these upstream parameters, is approximately 10 mHz.

261 **Acknowledgments.** The authors are grateful for thoughtful discussions with R. E. Denton
262 and J. G. Lyon.

References

- 263 Han, D. S., et al. (2007), Coupling of perturbations in the solar wind density to global Pi3
264 pulsations: A case study, *J. Geophys. Res.*, *112*(A05217).
- 265 Jacobs, J. A., Y. Kato, S. Matsushita, and V. A. Troitskaya (1964), Classification of geomagnetic
266 micropulsations, *J. Geophys. Res.*, *69*, 180.
- 267 Kepko, L., and H. E. Spence (2003), Observations of discrete, global magnetospheric oscil-
268 lations directly driven by solar wind density variations, *J. Geophys. Res.*, *108*(A6), 1257,
269 doi:10.1029/2002JA009676.
- 270 Kivelson, M. G., and D. J. Southwood (1985), Resonant ULF waves - A new interpretation,
271 *Geophys. Res. Lett.*, *12*, 49–52, doi:10.1029/GL012i001p00049.
- 272 Korotova, G. I., and D. G. Sibeck (1995), A case study of transient event motion in the magne-
273 tosphere and in the ionosphere, *J. Geophys. Res.*, *100*(A1), 35–46.

- 274 Lyon, J. G., J. A. Fedder, and C. M. Mobarry (2004), The Lyon–Fedder–Mobarry (LFM)
275 global MHD magnetospheric simulation code, *J. Atmos. Solar-Terr. Phys.*, *66*(15), 1333, doi:
276 10.1016/j.jastp.2004.03.020.
- 277 Matsuoka, H., K. Takahashi, K. Yumoto, B. J. Anderson, and D. G. Sibeck (1995), Observation
278 and modeling of compressional Pi 3 magnetic pulsations, *J. Geophys. Res.*, *100*(A7), 12,103–
279 12,115.
- 280 Sibeck, D. G., W. Baumjohann, R. C. Elphic, D. H. Fairfield, and J. F. Fennell (1989), The
281 magnetospheric response to 8-minute period strong-amplitude upstream pressure variations,
282 *J. Geophys. Res.*, *94*, 2505–2519, doi:10.1029/JA094iA03p02505.
- 283 Viall, N. M., L. Kepko, and H. E. Spence (2009), Relative occurrence rates and connection
284 of discrete frequency oscillations in the solar wind density and dayside magnetosphere, *J.*
285 *Geophys. Res.*, *114*(A13), 1201–+, doi:10.1029/2008JA013334.
- 286 Wiltberger, M., R. S. Weigel, W. Lotko, and J. A. Fedder (2009), Modeling seasonal variations
287 of auroral particle precipitation in a global-scale magnetosphere-ionosphere simulation, *J.*
288 *Geophys. Res.*, *114*(A13), 1204–+, doi:10.1029/2008JA013108.
- 289 Wright, A. N. (1994), Dispersion and wave coupling in inhomogeneous MHD waveguides, *J.*
290 *Geophys. Res.*, *99*, 159–167, doi:10.1029/93JA02206.

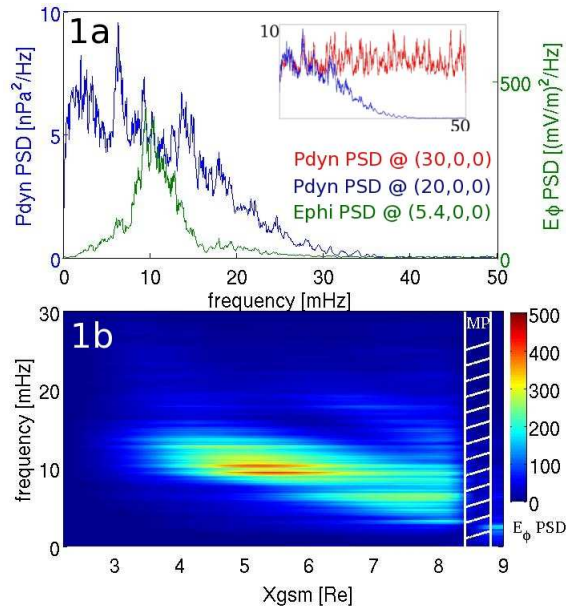


Figure 1. **a)** Dynamic pressure PSD in the upstream solar wind (blue trace) and E_{φ} PSD at $5.4 R_E$ on the noon meridian (green trace), from the continuum simulation. **Inset panel:** p_{dyn} PSD input at the LFM upstream boundary (red trace) and p_{dyn} PSD in the upstream solar wind (blue trace). **b)** E_{φ} PSD plotted along the entire noon meridian in the continuum simulation. The location of the magnetopause is indicated by the shaded region.

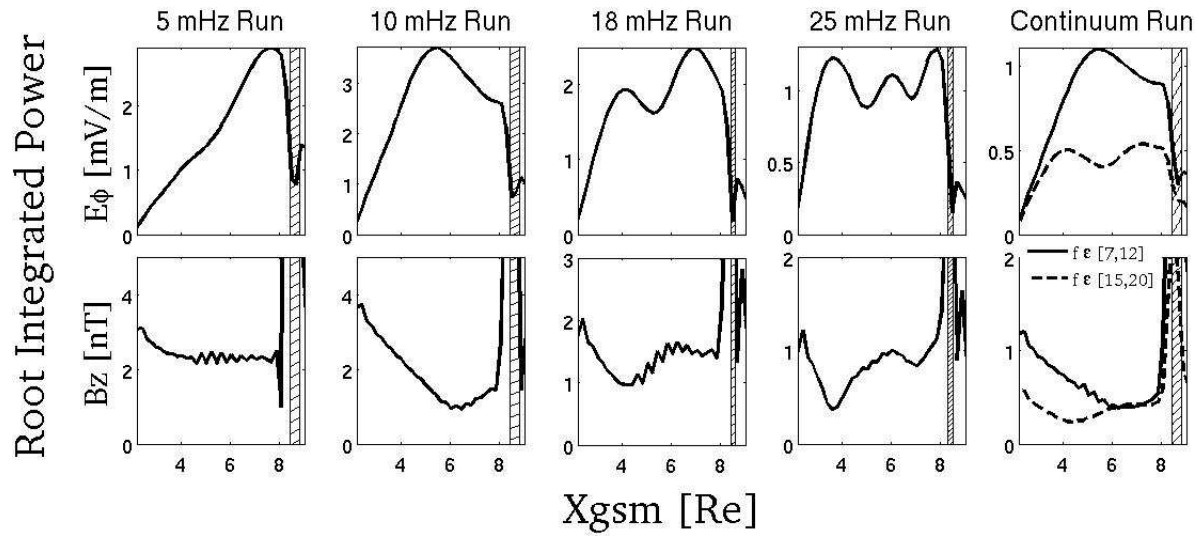


Figure 2. E_ϕ (top row) and B_z (bottom row) radial mode structure along the noon meridian for the five simulations (columns). RIP is integrated over the driving band in the monochromatic simulations (first four columns) and over [7,12] and [15,20] mHz in the continuum simulation (last column). The location of the magnetopause is indicated by the shaded region.